

Journal of Materials Chemistry A

Accepted Manuscript



This is an *Accepted Manuscript*, which has been through the Royal Society of Chemistry peer review process and has been accepted for publication.

Accepted Manuscripts are published online shortly after acceptance, before technical editing, formatting and proof reading. Using this free service, authors can make their results available to the community, in citable form, before we publish the edited article. We will replace this *Accepted Manuscript* with the edited and formatted *Advance Article* as soon as it is available.

You can find more information about *Accepted Manuscripts* in the [Information for Authors](#).

Please note that technical editing may introduce minor changes to the text and/or graphics, which may alter content. The journal's standard [Terms & Conditions](#) and the [Ethical guidelines](#) still apply. In no event shall the Royal Society of Chemistry be held responsible for any errors or omissions in this *Accepted Manuscript* or any consequences arising from the use of any information it contains.

Morphology Effects in Photoactive ZnO Nanostructures: Photooxidative Activity of Polar Surfaces

Ana Iglesias-Juez,^{1,*} Francesc Viñes,² Oriol Lamiel-García,² Marcos Fernández-García,¹ and
Francesc Illas,^{2,*}

¹ *Instituto de Catálisis y Petroleoquímica, CSIC, c/Marie Curie 2,
Cantoblanco, 28049 Madrid, Spain.*

² *Departament de Química Física & Institut de Química Teòrica i Computacional
(IQTUB), Universitat de Barcelona, c/Martí i Franquès 1, 08028 Barcelona, Spain.*

*corresponding authors: ana.iglesias@icp.csic.es, francesc.illas@ub.edu

Abstract

A series of ZnO nanostructures with variable morphology were prepared by a microemulsion method and their structural, morphological, and electronic properties were investigated by a combined experimental and theoretical approach using microscopy (high resolution transmission electron microscopy) and spectroscopic (X-ray diffraction, Raman, and UV-visible) tools, together with density functional theory calculations. The present experimental and computational study provides a detailed insight into the relationship between surface-related physicochemical properties and the photochemical response of ZnO nanostructures. Specifically, the present results provide evidence that light-triggered photochemical activity of ZnO nanostructures is related to the predominance of highly-active (polar) surfaces, in particular, the amount of Zn-terminated (0001) surfaces, rather than bandgap sizes, carrier mobilities, and other variables usually mentioned in the literature. Computational results highlight the oxidative capability of polar surfaces, independently of the degree of hydration.

Keywords: Photocatalysis • ZnO • Morphology • Density Functional Calculations • HR-TEM

1. Introduction

Wurtzite Zinc oxide (ZnO), also known as zincite, is a material of technological interest mostly due to its peculiar optical and electronic properties: ZnO displays high electron mobilities and thermal conductivities, and a direct bandgap (~3.4 eV) with large exciton binding energies (~60 meV),¹⁻³ stimulating its usage in a great deal of technological devices including semiconductors,⁴ field-effect transistors,⁵ photodetectors,⁶ blue- and UV-light emitting and laser diodes,⁷⁻⁹ gas sensors,¹⁰⁻¹² piezoelectric generators,¹³ transparent electrodes,¹⁴ and cells for solar light harvesting.¹⁵⁻¹⁷

As long as its chemistry is concerned, ZnO has recently become the focus of many research endeavours considering it as a possible catalyst for a variety of reactions.¹⁸ Apart from the long-standing use in rubber sulphur vulcanization,¹⁹ and its promoter key role in methanol synthesis when using the ternary copper-based Cu/ZnO/Al₂O₃ catalysts,²⁰⁻²² ZnO has been suggested as a suitable catalyst for water²³ and sulphur hydride²⁴ dissociations, desulfurization processes,^{25,26} the water gas shift reaction,²⁷ CO₂ activation,²⁸ and, finally, for the conversion of maleic anhydride into 1,4-butanediol.^{29,30}

At the overlap of the catalytic potential and the above-commented UV-light absorption capability one unfolds the photocatalytic aspect. ZnO has been a long-time posed material for light-triggered catalysis, with many studies even pointing a better quantum and reaction yield than Titanium oxide (TiO₂).^{31,32} The number of studies tackling the photocatalytic usage of ZnO bloomed in the last decade; mainly on dye decomposition³³⁻³⁶ but also for the treatment of volatile organic compounds,³⁷ peroxide synthesis,³⁸ water splitting,³⁹ and alcohol photodegradation.^{40,41}

Nevertheless, the photocatalytic process is far from being mastered, and the aspects governing the catalytic activity and selectivity are still a matter of debate. Hitherto many experimental works have addressed the issue of relating the photocatalytic activity with

structural factors by sampling a plethora of ZnO morphologies; from single crystal surfaces,⁴² to thin films,³⁵ powders,³² nanostructures featuring a great diversity of sizes and shapes (e.g. rods, disks, rings, screw caps, burgers, tubes, hourglass, trigonal prisms, toilet brushes, spheres, abalone shells, and so on),^{37,41,43-48} and, eventually, nanoparticles with well-defined facets.^{31,33,44,45} From such studies many aspects affecting the photochemical process can be invoked. For instance, concerning the acid brown 14 dye degradation, it has been shown that media acidity seems to affect the reaction, but, whereas a basic media enhances the yield for ZnO it hinders the yield for TiO₂ photocatalyst.³¹ Surprisingly, recent studies did not reveal any correlation between photochemical activity with neither nanoparticle size³³ nor surface area.⁴¹

Furthermore, relatively few of these studies analyse in detail the direct relation among ZnO morphology and the enhanced photocatalytic activity. The catalyst nanostructured morphology (primary/secondary particle size and shape) can be controlled depending on the synthesis method, the employed solvent, the addition of capping agents, and/or eventually the growing conditions.^{37,41,43,49} The synthesized oxide may feature distinct polar/nonpolar facet ratio depending on the experimental procedure, and this is often argued to be a key aspect on the photochemical catalytic activity. However, the discussion remains open to a large extent. On one hand, McLaren and coworkers³³ have shown that a higher proportion of polar surfaces, i.e. hexagonal disk-like nanoparticles, show a higher photocatalytic activity towards the methylene blue dye decomposition, in line with the results of Li *et al.* for the N-formylation of aniline.⁴³ In the former work³³ it is posed that the Zn-terminated (0001) polar surface is the responsible for the high catalytic activity, backed by the study of Xu and colleagues on phenol degradation.⁴¹

The idea behind such hypothesis is that such a surface—together with the O-terminated (000 $\bar{1}$)—is the most unstable one, i.e. exhibits the highest surface energy, and so

is prone to attach the reactants, although this explanation neglects the photochemical aspect. However, these and other authors^{33,41,43} also speculate on the possible critical role of surface oxygen vacancies on ZnO surfaces. Nonetheless, pristine polar surfaces suffer from an electric dipole instability issue, and in fact, do feature a variety of reconstructions which generally involve surface vacancies.^{50,51} Last but not least, although in some cases the role of nonpolar surfaces is ruled out,^{33,41} Kislov *et al.* have recently shown that the nonpolar surfaces of ZnO present the highest photochemical activity for the methyl orange dye degradation.⁴²

As long as the alcohol photodegradation is concerned, little is known on the key aspects governing the photocatalytic activity. Typically phenol is used as a probe molecule for liquid-phase photodegradation studies whereas isopropanol is the test case in the gas-phase counterpart.⁵² Regardless of that, isopropanol is commonly used as a liquid-phase hydroxyl scavenger additive.^{53,54} Previous studies on phenol photodegradation on ZnO nanostructures point that the Zn-terminated (0001) polar surface is the most catalytically active,⁴¹ and that ZnO nanoparticles exhibits a superior activity than TiO₂ ones.⁵⁵ This enhanced activity is also observed in the pioneering work of Kulkarni and Wachs on the photooxidation of isopropanol, in which it was found that ZnO selectively converts isopropanol into acetone *via* dehydrogenation.³² In this latter work the pivotal role of acid/basic sites on the catalytical activity and specificity was posed.

In the present work we explore the relationship between ZnO morphology and chemical activity in a series of nanometric samples and analyse the structural/electronic and chemical differences encountered for different nanostructures as a function of the specific surface planes exposed to the media, either naked or hydrated, but also, for polar terminations, including surface defects. To this end, ZnO wurtzite nanoparticles were synthesized by means of a microemulsion method and have been characterized by X-Ray Diffraction (*XRD*) patterns and High-Resolution Electron Microscopy (*HR-TEM*) images together with Density

Functional (*DF*) calculations on reliable model systems. The information obtained was used to rationalize the chemical properties exhibited by ZnO nanostructures in the photoelimination of isopropanol vapour. The structural and electronic characteristics of the polar/nonpolar faces are at the origin of the reactive response of ZnO nanoparticles but many details are, as above described, unknown. Here we attempt to address this issue and found evidence that the exposure of polar surfaces and, more explicitly, of Zn-terminated (0001) surfaces, is at the heart of the ZnO activity.

2. Experimental Section

2.1. Experimental Details

Materials were prepared using a microemulsion method using *n*-heptane (Scharlau) as organic media, Triton X-100 ($C_{14}H_{22}O(C_2H_4O)_n$) (Aldrich) as surfactant and hexanol (Aldrich) as cosurfactant. Zn was introduced from the nitrate from (Aldrich). Water/Zn molar ratio was fixed at 110 and water/surfactant molar ratio was varied from 54 (sample **A**), to 18 (sample **B**), and finally 9 (sample **C**). After introduction of Zn into the aqueous phase and 30 min of stirring, a double quantity of tetramethylammonium-hydroxide was introduced from the aqueous phase of a similar microemulsion. The resulting mixture was stirred for 24 h, centrifuged, and the separated solid precursors rinsed with methanol and dried at 110 °C for 12 h. The Brunauer-Emmett-Teller (*BET*) surface areas and average pore volume and sizes were measured by nitrogen physisorption (Micromeritics ASAP 2010). Samples present a *BET* area of 47, 25, and 23 m² g⁻¹ for **A**, **B**, and **C** materials, respectively. XRD profiles were obtained with a Seifert D-500 diffractometer using Ni-filtered Cu K α radiation with a 0.02° step and fitted using the Von Dreele approach to the Le Bail method.⁵⁶

HR-TEM was recorded on a JEOL 2100F TEM/STEM microscope. Specimens were prepared by dripping an ethanol suspension of the samples to be investigated onto a copper grid supporting a perforated carbon film. Raman spectroscopy was also carried out to explore

the structural characteristics of the ZnO nanostructures. Raman spectra were acquired using a Horiba iH320 spectrometer and He:Ne laser excitation (632.8 nm). UV-visible diffuse reflectance spectroscopy experiments were performed with a Shimadzu UV2100 apparatus with a nominal resolution of ca. 1 nm using BaSO₄ as reference. Band gap analysis was carried out following standard procedures (for a direct band gap semiconductor) by plotting $(h\nu A)^2$ (where $h\nu$ = excitation energy and A = absorption coefficient) vs. energy.

2.2. Computational Details

Different slab models have been constructed to simulate the ZnO nanoparticle facets. From present (see below) and previous XRD studies^{16,33,37,41,45} it is clear that wurtzite ZnO preferentially displays the nonpolar (10 $\bar{1}$ 0) and (11 $\bar{2}$ 0) surfaces, and the Zn- and O-terminated (0001) and (000 $\bar{1}$) polar surfaces, respectively. Nonpolar surfaces can perfectly feature an unreconstructed termination whereas polar surfaces suffer from a well-known surface energy instability issue. Considering ZnO as an ionic material (with the caveat that is in the fringe region of ionic compounds), the different charged terminations of the polar surfaces exhibit a net dipole moment, which *de facto* increases with the separation between them. This introduces an electrostatic component to the surface energy that diverges with the surface separation.^{57,58}

There are various ways to nullify this dipole moment. The bulk cut termination may exist involving a charge transfer from electron-rich O-terminated (000 $\bar{1}$) surface to electron-poor Zn-terminated (0001) surface. However, despite such charge transfer is feasible for systems with few layers, it becomes unrealistic for the systems here contemplated. So, for nanometer-sized ZnO (0001)/(000 $\bar{1}$) systems it has been found that pristine terminations must feature 1/4 ML of surface vacants to compensate the under/overcharge.⁵⁹ Many previous studies reveal a variety of surface reconstructions as a function of the O₂ and H₂ pressure.^{50,51,60} Aside from this, it has been found that when fully hydrogenated/hydrated both

polar surfaces show a perfect (1×1) arrangement, i.e. apparently no surface defects.⁶¹⁻⁶³ Because of this, we decided to consider the ideal pristine polar surface models only as a conceptual reference for dehydrogenation/dehydration processes, thus allowing for decoupling the desorption from surface reconstruction (vacancy formation) process.

To ascertain how the electronic structure affects the photochemical activity we investigated pristine nonpolar surfaces and polar surfaces with surface vacants. Moreover, following previous investigations,⁶⁴ we considered also fully hydrated ZnO surfaces, e. g. saturation coverage which imply one half coverage of surface Zn atoms by hydroxyls on (0001) surface, one half coverage of surface O atoms by H on (000 $\bar{1}$) surface, a mixed H₂O dissociated situation for nonpolar (10 $\bar{1}$ 0) surface, and a fully dissociated situation for nonpolar (11 $\bar{2}$ 0) surface, the latter being these the most stable situations. These also feature almost the same density of adsorbed water molecules per surface area —fragments, *i.e.*, hydroxyl and atomic H groups coming from a water molecule scission in the case of polar surfaces—, in particular, 0.05 fragments Å⁻² for (0001)/(000 $\bar{1}$) polar surfaces, and 0.06 and 0.07 H₂O molecules Å⁻² for (10 $\bar{1}$ 0) and (11 $\bar{2}$ 0) surfaces, respectively. Further details on these structures and their stability are found in Ref. 64 and references therein. Note in passing by that surface slab models were constructed, for the sake of convenience, from the orthorhombic bulk unit cell, sketched in Figure 1, containing 8 atoms (4 O + 4 Zn) instead of the usual hexagonal bulk unit cell, containing 4 atoms (2 O + 2 Zn).

Following a widely-used computational scheme, 8-layer slabs have been used to represent each of the four surfaces, in which the upmost four layers are completely allowed to relax whereas the bottommost four layers are kept fixed as in the bulk-optimized positions — *a.k.a.* 4+4 approximation—. Present tests and several past studies by different working groups reveal that such slab width and relaxation approximation is enough to ensure converged

results of surface properties.⁶⁵⁻⁷⁵ Note however that cleavage energies of polar surfaces are actually derived with an extrapolation to infinite slab thickness.^{66,67,69}

Vacant-free pristine surfaces have been modeled using (1×1) primitive unit cells. For polar surfaces containing vacancies and hydrated surfaces larger supercells have been employed. The (001) polar surfaces simulating 1/4 vacancies on both O- and Zn-terminations have been constructed using a (1×2) supercell based on the orthorhombic cell depicted in Figure 1, which relates to the primitive $p(1\times 1)$ unit cell through the $\begin{pmatrix} 2 & 0 \\ -1 & 2 \end{pmatrix}$ matrix transformation of the unit cell vectors. For both terminations, this supercell contains four surface atoms and, for each termination, one surface atom has been removed, thus modeling the 1/4 vacancy concentration at each termination, while maintaining the ZnO stoichiometry as well. The 1/2 coverage of hydroxyls on (0001) surface and the 1/2 coverage of H on (000 $\bar{1}$) surface has been modelled using the (1×1) orthorhombic unit cell obtained from the primitive one through a $\begin{pmatrix} 1 & 0 \\ -1 & 2 \end{pmatrix}$ matrix transformation.

The H₂O mixed dissociated situation on nonpolar (10 $\bar{1}$ 0) surface, as profusely studied both experimentally and theoretically, has been modeled using a (2×1) unit cell,^{64,76,77} whereas a (1×1) unit cell is adequate for the full dissociated situation on nonpolar (11 $\bar{2}$ 0) surface.⁶⁴ A minimum vacuum of 1 nm was applied in the surface direction to avoid interaction between repeated slabs. A counterdipole was set in the middle of the vacuum gap to compensate long-range dipole-dipole interactions among repeated slabs for pristine polar surfaces. An optimal Monkhorst-Pack **k**-points grid of 17×17×1 has been used for the ZnO surface calculations, guaranteeing an energy convergence below 0.01 kJ mol⁻¹ as tested using denser grids.

Present DF calculations were performed with the VASP code,⁷⁸ carrying out periodic Kohn-Sham calculations for the above-described surface slab models. The projector

augmented wave method has been used to represent atomic cores effect on the valence electron density.⁷⁹ This representation of the core states allows one to obtain converged results —variations in energy below 0.01 kJ mol^{-1} — with a cut-off kinetic energy of 415 eV for the plane-wave basis set. Geometry optimizations were performed using a conjugated gradient algorithm and applying a tetrahedron smearing method with Blöchl corrections. The structural optimization was finalized when forces acting on atoms were below $0.01 \text{ kJ mol}^{-1} \text{ pm}^{-1}$. Unless stated otherwise, all calculations were carried out in a non spin-polarized fashion. All DF calculations have been carried out using the Perdew-Burke-Ernzerhof (*PBE*) exchange correlation (*xc*) functional.⁸⁰ This *xc* functional has proven to deliver a realistic description of bulk ZnO and low-index Miller surface structures.^{61,65,66,69}

Note that PBE, among other *xc* functionals, severely underestimates materials bandgap. Indeed, the bandgap for ZnO is here computed to be 0.83 eV, quite small compared to experimental value of 3.4 eV,¹⁻²³ but in line with previous PBE values of 0.83 eV of Alkauskas and Pasquarello,⁸¹ and of 0.9 eV of Moreira *et al.*⁸² This drawback can be compensated by using hybrid *xc* functionals, in which the incorporation of Hartree-Fock exchange counteracts this deficiency. For instance, ZnO bandgap calculated using the Becke-Lee-Yang-Parr (*B3LYP*)⁸³ *xc* is 3.34 eV,⁸⁴ quite close to the experimental value. Another way of solving this issue is to carry many body GW calculations, which deliver a bulk ZnO value of 3.08 eV.⁸⁵ More importantly, a direct proportionality of GW and PBE bandgap values was found in this latter study, which, applied to our calculated value, provides a bandgap of 3.32 eV, quite close to the experimental value. This allows discussion of computationally more economic PBE-based bandgaps, which are nevertheless connected to correct values.

Surface energies have for the (4+4) slabs have been obtained following a procedure detailed in the past (see *e.g.* Ref. 86). In summary, the surface energy of the truncated bulk slab, γ^{fix} is defined as;

$$\gamma^{fix} = \frac{E_{slab}^{fix} - E_{bulk}}{2A} \quad (1)$$

where E_{slab}^{fix} is the total energy of the slab unit cell containing two equal surfaces, and E_{bulk} is the total energy of the slab atoms in bulk environment. A is the area of each surface created within the slab unit cell. Given that γ^{fix} is known, one can extract the surface energy of a relaxed surface, γ^{rel} , from the following equation;

$$\gamma^{rel} = \frac{E_{slab}^{rel} - E_{bulk}}{A} - \gamma^{fix} \quad (2)$$

where E_{slab}^{rel} is the total energy of the relaxed slab —here with only one its surfaces being relaxed—. Alternatively, one could calculate the relaxation energy per unit area, γ^{relax} according to;

$$\gamma^{relax} = \frac{E_{slab}^{rel} - E_{slab}^{fix}}{A} \quad (3)$$

and then adding the relaxation energy to γ^{fix} .

Thus, this procedure for computing surface energies is valid for the nonpolar surfaces and for asymmetric employed slabs. However, it cannot be used for polar surfaces because, inevitably, both surface terminations are different and present in the slab calculation. For the polar surfaces where both terminations are relaxed we define the cleavage energy, E_{cleav} , defined as:

$$E_{cleav} = \frac{E_{slab}^{rel} - E_{bulk}}{A} \quad (4)$$

Note that within this definition relaxed surface energies of nonpolar surfaces equal to half of their cleavage energy. For this latter systems, both surface and cleavage energies are well converged —variations below 0.1 J m^{-2} — already for a slab thickness of 8 layers.⁸⁷ For the polar surfaces cleavage energies have been calculated for various slab thicknesses —up to 14 layers, each layer containing a ZnO unit— where all atomic layers were relaxed. The given

value is extrapolated to infinite thickness, following a procedure described elsewhere.⁶⁵⁻⁶⁷ For any nonpolar surface, fully hydrated surface energy, γ^{H_2O} , has been calculated by subtracting the water adsorption energy, $E_{ads}^{H_2O}$, per A area unit. Values are taken from a previous study using same computational level.⁶⁴

$$\gamma^{H_2O} = \gamma^{rel} - \frac{E_{ads}^{H_2O}}{A} \quad (5)$$

The fully hydrated cleavage energy, $E_{cleav}^{H_2O}$, of polar (0001)/(000 $\bar{1}$) surfaces have been obtained similarly, although the H₂O adsorption energy has been introduced assuming that OH groups are solely adsorbed on (0001) surface, whereas H groups are adsorbed on (000 $\bar{1}$) surface. Thus;

$$E_{cleav}^{H_2O} = E_{cleav} - \frac{E_{ads}^{OH/(0001)} + E_{ads}^{H/(000\bar{1})}}{A} \quad (6)$$

Electron/hole pair conductivity is explained based on the their effective masses, estimated in a first approximation assuming a parabolic dispersion of Conduction Band (CB) maximum and Valence Band (VB) minimum, in the form;

$$E(\mathbf{k}) = \frac{\hbar^2 |\mathbf{k}|^2}{2m^*} \quad (7)$$

where $E(\mathbf{k})$ is the band energy around its stationary point, here arbitrarily defined as $\mathbf{k} = 0$, i.e. at Γ point; \hbar is the reduced Planck constant, \mathbf{k} is the \mathbf{k} -vector distance, and m^* is the effective mass. In this sense, the effective masses are obtained from the curvature of the band minima or maxima adjusted to a second degree polynom, as done in previous related studies.⁸⁸ For that, the bandstructure within the irreducible Brillouin zone has been sampled from Γ point — at which direct band gap is found— towards \mathbf{A} , \mathbf{M} , and \mathbf{K} points, which correspond in real space to [0001], [10 $\bar{1}$ 0], and [11 $\bar{2}$ 0] directions, see Figure 1. During the bandstructure sampling a \mathbf{k} -point density of 0.02 points nm⁻¹ or better was used.

The electronic structure has been also studied based on the Density Of States (*DOS*) or, more specifically, the projected *DOS*. In this case, an energy resolution of 0.05 eV was employed, and the projection was carried out over the surface and near surface atoms, including the adsorbates upon when found. For a proper comparison of VB and CB of the different surfaces and situations, the bands were aligned using the vacuum energy level as zero energy reference.

3. Results and Discussion

The XRD patterns of ZnO samples obtained with the microemulsion method by varying the surfactant to water ratio are shown in Figure 2. Table 1 summarizes some characterization results obtained from XRD and other techniques and concerning structural and morphological properties. All synthesized samples present XRD pattern ascribable to the characteristic wurtzite ZnO structure,⁸⁹ and their average primary particle size diminished with the increase of the surfactant agent concentration used during the microemulsion method (Table 1). More importantly for our purposes, we can see that the $(10\bar{1}0)/(0002)$ XRD intensity ratio varies from 0.69 for sample **B** to 0.89 for sample **C** evidencing a morphology modification among the sample series. A decrease of such ratio indicates a morphology variation in which the stacking along the crystallographic *c* axis is favoured, consequently leading to an increase in the extension of nonpolar planes at the surface, or, viewed from another perspective, to a decrease of the polar vs. nonpolar surface extension. According to present XRD results the proportion of polar surfaces would grow from sample **B** to **A** and then become maximum for **C**.

Such morphology evolution throughout our sample series was studied in detail using HR-TEM. The TEM images of the sample with higher surfactant concentration, **A** (Figure 3a), show rounded (hexagonal-like) ZnO nanoparticles with sizes around 5 nm. Decreasing of surfactant concentration leads to increasing average particle size (Table 1) and a drastic effect

on shape (Figure 3). Sample **B** present more elongated forms (Figure 3b) while those in sample **C** displays sharp needle-like structures (Figure 3c). Extra images from other individual crystals of the studied samples show that the present results are representative of other areas and a valid statistical impression, as shown in the Supplementary Information.

For sample **A**, hexagonal-disk type morphology becomes more evident from high resolution images. Figure 4a shows a magnified HR-TEM image and the corresponding Fast Fourier Transform (*FFT*) diffraction pattern for the selected area. The analysis of FFT diffractions patterns indicates a $[0001]$ zone axis and consequently the ZnO-disk morphology mainly exposing at the surface layer polar $(0001)/(000\bar{1})$ planes and, in less proportion, $(10\bar{1}0)$ facets. For a brick-type morphology like in sample **B**, high resolution image and the corresponding FFT diffraction pattern (Figure 4b) indicate the presence of well-defined nanostructures displaying a $[10\bar{1}0]$ zone axis, similar to those found in the literature.⁴⁵ This would correspond to slightly elongated particles along the *c* crystallographic orientation and presenting larger contribution of nonpolar $(10\bar{1}0)$ than polar $(0001)/(000\bar{1})$ plane types. Figure 4c presents HR-TEM images for sample **C** and the corresponding FFT diffraction pattern of the selected zone of the needle entities. The analysis unequivocally identifies a $[0001]$ zone axis, so the nanostructure grows in a direction perpendicular to the crystallographic *c* axis exposing polar $(0001)/(000\bar{1})$ and nonpolar $(10\bar{1}0)$ facets along the needle particulate surface layer. The analysis is representative to the other crystals present in the samples, as shown in the Supplementary Information.

The TEM analysis provides a clear view of the morphology evolution among our samples. The anisotropic growth evidenced in the XRD patterns is then clarified using the TEM analysis (Figs. 3 and 4). Such morphology differences are customarily justified on the basis of the different surface free energies of the crystallographic planes. During nucleation and growth at preparation states, a fast growing plane generally tends to disappear or has

limited expression/extension at the end of the preparation, allowing larger expression of slow growing planes, typically having lower surface energy.⁹⁰

To support this, DF based calculations of the surface energies have been carried out, although, for the present purposes, a more important quantity is the estimated cleave energies, following the procedure above-described. Thus, DF cleavage energies for the vacant-free (0001)/(000 $\bar{1}$), (11 $\bar{2}$ 0), and (10 $\bar{1}$ 0) surfaces, are, respectively, 3.31, 1.78, and 1.70 J m⁻². Note that the cleavage energy of the polar surfaces is very close to those previously reported^{65,66} at PBE level of 3.41 J m⁻² and goes along with the infinite thickness slab B3LYP value of ~ 4 J m⁻².⁶⁷ The calculated cleavage energies of the (11 $\bar{2}$ 0) and (10 $\bar{1}$ 0) surfaces are very similar to previous PBE results⁶⁶ of 1.7 and 1.6 J m⁻², respectively. Furthermore, present results match the preference in stability of (10 $\bar{1}$ 0) surface with respect to the (11 $\bar{2}$ 0) by ~ 0.1 J m⁻².⁶⁶

According to this, in the low water (high surfactant) regime, such as in sample **A**, most stable structure should feature small pristine polar (0001)/(000 $\bar{1}$) facets, and large nonpolar (10 $\bar{1}$ 0) and (11 $\bar{2}$ 0) facets. Based on these results and, as generally reported, the growth of ZnO crystals preferentially would occur along the [0001] direction to form rod-like structures, which is not the case in our samples. The explanation arises when computing realistic models of polar surfaces with vacancies. Present value of cleavage energy for (0001)/(000 $\bar{1}$) surface containing 1/4 vacancies is 1.07 J m⁻². This would suggest that (0001)/(000 $\bar{1}$) facets containing vacancies would be the most exposed surface, with lower ratio of nonpolar planes. This matches hexagonal nanodisk structures obtained at high surfactant concentration employed in the preparation of sample **A**, which dominantly exposes polar (0001) and (000 $\bar{1}$) surfaces.

However the fully hydrated cleavage energies explain a different tale: They are, for vacant-free (0001)/(000 $\bar{1}$), (11 $\bar{2}$ 0), and (10 $\bar{1}$ 0) surfaces, respectively, 0.76, -0.31, and -0.34 J m⁻². Thus, this reveals that in systems with more water content —like in sample **B**— all

surfaces can become hydrated and consequently further and strongly stabilized. It is worth to note that in such conditions the largest stabilization results for nonpolar surfaces, and therefore, these should be the ones most exposed. This matches the brick-wall structures of sample **B** obtained using standard water/oil values (e.g. a ratio between 12 and 20) of microemulsion parameters.⁹¹ The elongated nanocubes predominantly expose nonpolar ($11\bar{2}0$) and ($10\bar{1}0$) surfaces, in perfect agreement with the order of stability of the different surfaces as derived from DF calculations (Figure 3).

It is known that the use of capping agents may play a key role in morphology control. Depending on the nature of the capping molecules, they can be preferentially adsorbed in different ZnO surfaces. These adsorbed moieties can prevent contact between the growth units at particular surfaces and thus, direct the growth in other spatial directions. A large number of studies published in this field support this statement.^{20,21} For example, citrate anions with COO^- and -OH groups are preferentially adsorbed on the positively charged Zn terminated (0001) surface, preventing contact between the growth unit and the (0001) crystal surface. Under these conditions, ZnO crystal would grow primarily along the other six symmetric directions (the so-called preferential equatorial growth).

This is a reasonable explanation for the morphologies obtained in sample **C**, which otherwise, due to the low surfactant concentration —water saturation conditions— should feature completely water saturated surfaces, and a morphology similar to sample **B**. However, in **B** the growth appears to be governed by the thermodynamics, whereas in **C** kinetics seems to play a key role. Take for instance a ZnO nanoparticle with all surfaces fully hydrated due to the capping effect of H_2O , OH , or H moieties. In order to grow in a particular surface direction, a moiety must desorb of the surface to allow a ZnO growing unit to be inserted. Desorption can be difficult in water rich conditions, *i.e.* the desorbed water molecule can

easily be replaced by another water molecule. However, the limiting step seems to be still the desorption energy.

In the case of (0001)/(000 $\bar{1}$) polar surfaces the desorption is more problematic; on one hand, it would imply desorption of hydroxyls from the (0001) surface, or H atoms in the (000 $\bar{1}$) case. Here we conceptually considered the simultaneous desorption of both moieties from both surface terminations to form a water molecule in the media, and thus, leaving both surfaces free to further grow, thus allowing a more fair comparison with the other surfaces. On the other hand, moiety desorption is considered leaving the polar surfaces naked and pristine, *i.e.* free of vacancies. This is done because when fully hydrated, polar surfaces are found to feature a regular vacant-free (1 \times 1) pattern.⁶¹⁻⁶³ Therefore, we decided to separate desorption from a possible posterior vacancy formation process, which is out of the present discussion. One must keep in mind, however, that when water would be removed from the polar surfaces, they would unavoidably reconstruct forming vacancies. Given said that, present calculations reveal desorption energy to be 2.55, 2.04, and 2.09 J m⁻², for vacant-free (0001)/(000 $\bar{1}$), (10 $\bar{1}$ 0), and (11 $\bar{2}$ 0) surfaces. Thus, capping effect is largest on polar surfaces, fact that explains why sample C presents principally (0001) and (000 $\bar{1}$) surfaces with even a largest polar/nonpolar facet ratio than sample A.

Having explained the morphology based on the synthesis media and growing conditions, we now focus on the photocatalytic aspect. For isopropanol photooxidation it is well known that the initial radical attack is carried out by hole-related species.⁹² The alcohol degradation assisted by UV light irradiation is based on the principle that UV light creates electron/hole (e⁻/h⁺) pairs within the semiconductor. Holes generated in the VB are capable of oxidizing the alcohol substrate and the CB electrons are capable of reducing oxygen present in air. The generated e⁻/h⁺ pairs suffer competitive fates concerning their recombination or

involvement in chemical steps. The efficient separation of photogenerated electron/hole is one of the important factors in the reaction.

As well-known, the relative energy of VB and CB levels determines the (potential) transfer path(s) of photoexcited holes and electrons, which can directly influence their fate as charge recombination and/or chemically related species. Primary size and shape are important morphological parameters affecting photoactivity by influencing VB and CB levels. Size is rather important but the crystalline dimension range here explored (Table 2; average dimension between 4 and 8 nm) would indicate that changes in valence and conduction band edge positions are rather limited.⁹³ In fact, calculation of the band gap in our samples using UV-visible data gives a constant value within experimental error (Table 1). It thus seems that here shape would be an important morphological aspect driving chemical performance of charge carriers. Shape effects in photocatalysis of TiO₂ and ZnO have been the subject of a significant number of publications, summarized in recent review articles,^{94,95} and here we focus on the specific grounds of this important issue.

Electron/hole effective masses for bulk wurtzite ZnO along (0001), (10 $\bar{1}$ 0), and (11 $\bar{2}$ 0) directions have been calculated following the procedure detailed in the Methods section for the orthorhombic wurtzite bulk cell (Figure 1), and values are encompassed in Table 2. Results indicate that charge mobility has no significant differences (maximum of ca. 10%) as a function of the orientation. However, DF calculations performed to estimate the CB and VB bands based on DOS of the different hydrated surface facets (Figure 5) show a different energy ordering for VB end- and CB start-edges: The VB end-edge of the facets of ZnO crystals follows the order (0001) > (000 $\bar{1}$) > (10 $\bar{1}$ 0) > (11 $\bar{2}$ 0), and, on the contrary, the corresponding CB end-edge follows an inverse order of (11 $\bar{2}$ 0) < (10 $\bar{1}$ 0) < (000 $\bar{1}$) < (0001). In the case of pristine nonpolar surfaces and polar surfaces displaying a concentration of 1/4 of vacancies, the ordering is similar; the VB end-edge follows the trend (0001) > (000 $\bar{1}$) ~

$(10\bar{1}0) > (11\bar{2}0)$, and so the inverse order for CB end-edge, $(11\bar{2}0) < (10\bar{1}0) \sim (000\bar{1}) < (0001)$, see Supplementary Information.

Indirectly the VB plots in Figure 5 show that work function values for different surface terminations differ within a range of 1.2 eV, which is in line with variations of up to 0.8 eV as found in the literature.⁹⁶ Note that the ZnO work function is generally accepted to be around 4.3 eV, as found for nanocrystalline thin films.⁹⁷ Indeed, variations between different surface terminations are well below this value, and also smaller than the changes in the work function produced by adsorption of polar molecules upon, found to vary the work function by up to 2.9 eV.⁹⁸⁻¹⁰⁰

Coming back to Figure 5, it indicates that the (0001) facets are those that feature the maximum stabilization of photogenerated holes, followed by the $(000\bar{1})$ surface. Compared to $(10\bar{1}0)$ and $(11\bar{2}0)$ facets, holes are more stable at these polar surfaces thereby making them more prone than the nonpolar ones to photooxidation steps involving organic compounds. On the other hand, electrons are more stable on nonpolar surface, suggesting that these constitute better active sites for photoreduction. This argument holds for fully hydrated surfaces, but, as shown in the Supplementary Information, such hole/electron stability is maintained on dehydrated surfaces as well. Thus, one could argue that such difference in stability is kept at any degree of ZnO nanoparticle surface hydration.

Note that holes/electrons would be generated on all the surfaces, although a transfer among surfaces would be favorable given the different stability. If such a transfer would not be inhibited, holes would accumulate polar surfaces, and electrons on nonpolar ones. Thus, the presence of both types of surfaces would allow the photogenerated e^-/h^+ pairs to be separated for a longer time, hindering the recombination rate and making ZnO more effective in the photocatalytic degradation of isopropanol. However such hypothesis neglects the dipole energy barriers to be overcome at junctions between surfaces, the band bending, and also

charge unbalance effects. These as well as dynamical aspects are no doubt of interest but they are out of the scope of the present work, and will require further investigation.

Experiments have been carried out on samples A-C to rule out first inhomogeneity issues in between samples. Raman scattering is an effective technique to investigate the crystallization, structure, and defects in nanostructured materials. Measurements were performed on different points of these materials to check homogeneity and it was observed that Raman spectra thus recorded are rather similar. According to group theory, hexagonal wurtzite ZnO belongs to P63mc space group, the optical phonons at the Γ point of the Brillouin zone are $A_1 + 2B_1 + E_1 + 2E_2$. Both A_1 and E_1 modes are polar and split into transverse TO and longitudinal optical LO phonons and are Raman active, whereas the B_1 modes are Raman inactive (silent modes). The two non-polar E_2 modes (E_{2low} , E_{2high}) are only Raman active. Figure 6 shows the Raman spectra for the three samples discussed in this work. A sharp peak at 433-453 cm^{-1} can be assigned to the E_2 high mode of non-polar optical phonons, which is the characteristic peak of the hexagonal wurtzite phase. Other E_2 related mode peaks appear at 90 cm^{-1} (E_{2low}), 195 cm^{-1} ($2E_{2low}$) and 331-327 cm^{-1} to ($E_{2high}-E_{2low}$), the last two due to multiple phonon scattering processes. The peak at 383 cm^{-1} corresponds to A_1 transverse optical (TO) mode. A small peak at 580 cm^{-1} attributed as the E_1 (LO) mode has also been observed. Generally, it is believed that the E_1 (LO) mode is related to the structural defects (oxygen vacancies, zinc interstitials, free carriers, etc.) in ZnO. The low intensity of the E_{2high} peak and the absence of significant differences among the presented spectra suggest that the samples exhibit well crystalline hexagonal wurtzite entities without substantial differences in lattice/defect related structural properties.

Last, Figure 7 presents the normalized photooxidation rate of the samples (e.g. rates eliminating the effect of the different surface area of the samples) as a function of the $(10\bar{1}0)/(0002)$ XRD intensity ratio. A “natural” order evolves from this graph; needle crystals

(sample C) showing much higher activity than flat crystals (sample A), and these two structures displaying larger activity than brick structures (sample B). These results highlight the requirement of the presence of polar surfaces for obtaining high photocatalytic performance. This, in combination with present DF-based photochemical activity trends, and considering, as above-mentioned, the h^+ key role in the process, indicates that isopropanol photoelimination is likely to occur on polar ZnO nanoparticle facets, independently of the degree of hydration. In particular, Zn-terminated (0001) surface is the one with *a priori* better photooxidation activity. This rules out the effect of water displacement by isopropanol as a key factor.

Thus, apparently, the exposure of polar surfaces, in particular the Zn-terminated (0001) surface, appears to be a key factor for the photooxidation capability of ZnO nanostructures. This results further supports the previous work of Maclaren and coworkers,³³ showing that a higher proportion of polar surfaces is needed for a good organic compound decomposition, although here needle-like structures show a better activity than previous³³ and present hexagonal disk-like nanoparticles. Aside, the key role of (0001) surfaces is also in line with previous studies on alcohol degradation.⁴¹ This shows why sample C, showing the higher ratio of (0001) surfaces, maximizes the isopropanol photooxidation rate as seen in Figure 7. To obtain such a high ratio of polar surfaces, one needs to synthesize ZnO nanoparticles in a water rich environment. Thus, this shape comparison in equal conditions allows one to figure which polar surface is best to improve the photocatalytic power of a ZnO-based nanoparticle material.

4. Conclusions

A series of ZnO nanostructures were prepared by microemulsion using a single pot procedure. A multitechnique XRD, Raman, TEM, UV-visible experimental study combined with DF calculations allowed us to provide a complete structural, morphological, and

electronic analysis of the materials. The nanostructured ZnO entities displayed disk-, brick-, and needle-like morphologies as the surfactant to water ratio of the microemulsion procedure continuously decreases from ca. 60 to 10 values.

The analysis of the chemical response of such ZnO nanostructures in the photoelimination of isopropanol was rationalized in terms of the structural/electronic properties of the nanosolids. The combined experimental and theoretical approach was able to provide evidence that the process is better carried out on polar surfaces, independently on the degree of hydration, and consequently, ruling out the effect of water displacement by isopropanol adsorption. Furthermore, the key role played by the ratio between polar and nonpolar facets exposed at the external surface of the ZnO nanomaterial is disclosed. It is shown that maximization of activity is not obtained by physicochemical properties (e.g. defects, band gap energy, etc.) previously described in the literature, but by maximizing the exposure to the external solid surface of polar surfaces in general, and ZnO Zn-terminated (0001) surface in particular. This is shown to be grounded in the preferential stability of holes upon light excitation at (0001) surfaces. This feature would be relevant for all photodegradation processes and thus hold general validity for ZnO nanomaterials.

Acknowledgements

We are indebted to one of the reviewers for truly enlightening discussion beyond that required in usual peer review reports, the referee comments have been crucial to reach a physically sound interpretation. Authors also thank Dr. A.B. Hungría for discussion of TEM results. Financial support by Spanish MICINN/MINECO research grants CTQ2010-14872/BQU and CTQ2012-30751 and, in part, by *Generalitat de Catalunya* grants 2014SGR97 and XRQTC is acknowledged. O.G.L. thanks the *Universitat de Barcelona* for a predoctoral APIF fellowship; F.V. and A.I.J. thank the MINECO for a postdoctoral *Juan de la Cierva* grant (JCI-2010-06372) and for a postdoctoral *Ramón y Cajal* contract, respectively. F.I. acknowledges additional support from the 2009 ICREA.

Table 1 Water to surfactant molar ratio microemulsion parameter values (w), primary particle size (Size, in nm) calculated from XRD data, and BET areas (A_{BET} , in $\text{m}^2 \text{g}^{-1}$), $(10\bar{1}0)/(0002)$ diffraction peaks intensity (I) ratio, and band gap energy (eV) measured from UV-visible data.

Parameter/Sample	A	B	C
w	9	18	54
Size	4.1	7.5	8.5
A_{BET}	35	25	23
I	0.78	0.69	0.89
Band gap	3.35	3.33	3.31

Table 2 Lighthole (m^h) and electron (m^e) effective masses, in units of free electron effective mass, $1 \cdot 10^{-2} m_0$, for wurtzite ZnO along [0001], $[10\bar{1}0]$, and $[11\bar{2}0]$ directions, and averaged bulk value.

Direction	[0001]	$[10\bar{1}0]$	$[11\bar{2}0]$	Bulk
m^e	0.37	0.37	0.42	0.38
m^h	0.40	0.45	0.41	0.42

Figure 1.- Crystallographic wurtzite bulk ZnO on the orthorhombic unit cells showing the preferential surface orientations (upper image) and the corresponding reciprocal unit cell (lower image).

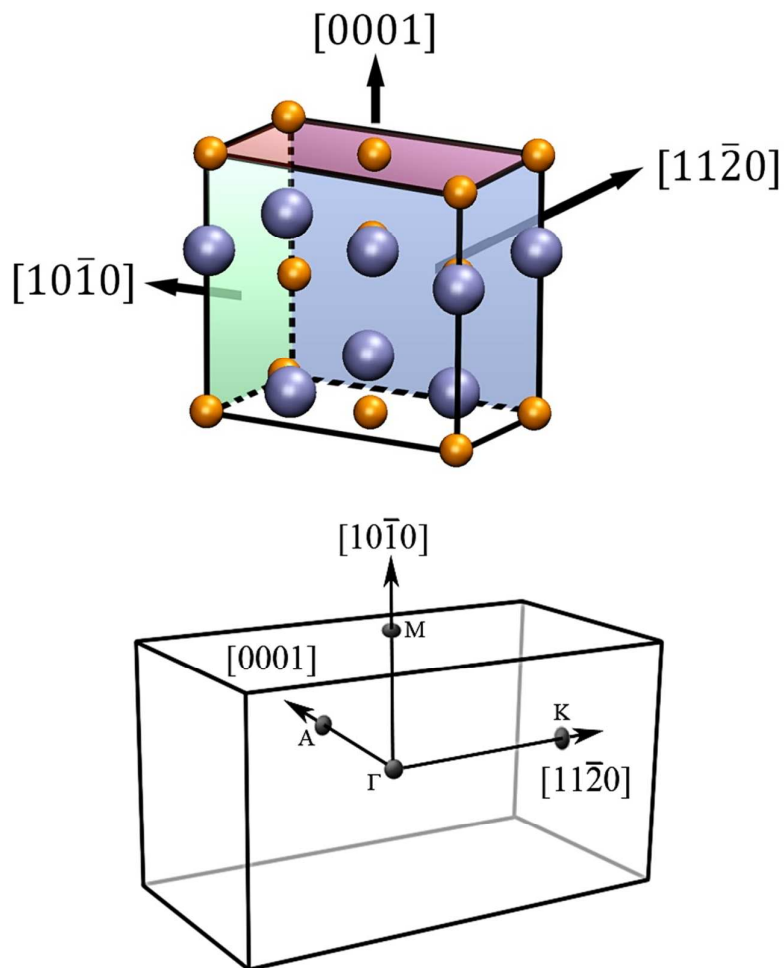


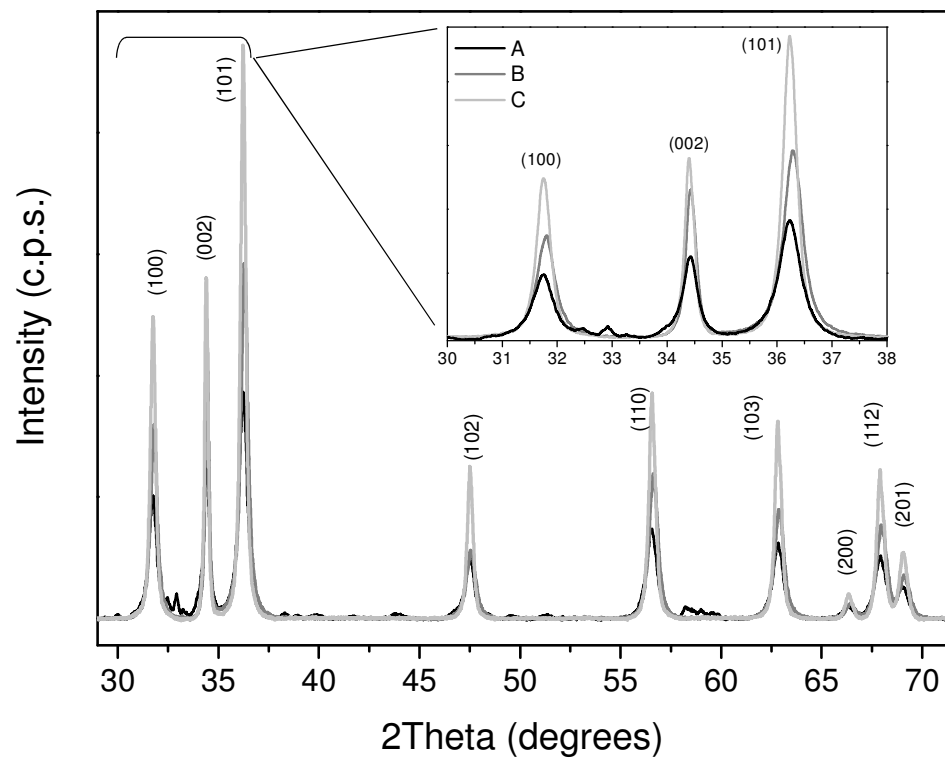
Figure 2 .-XRD patterns of the synthesized **A**, **B**, and **C** samples.

Figure 3.- TEM images corresponding to samples A, B, and C.

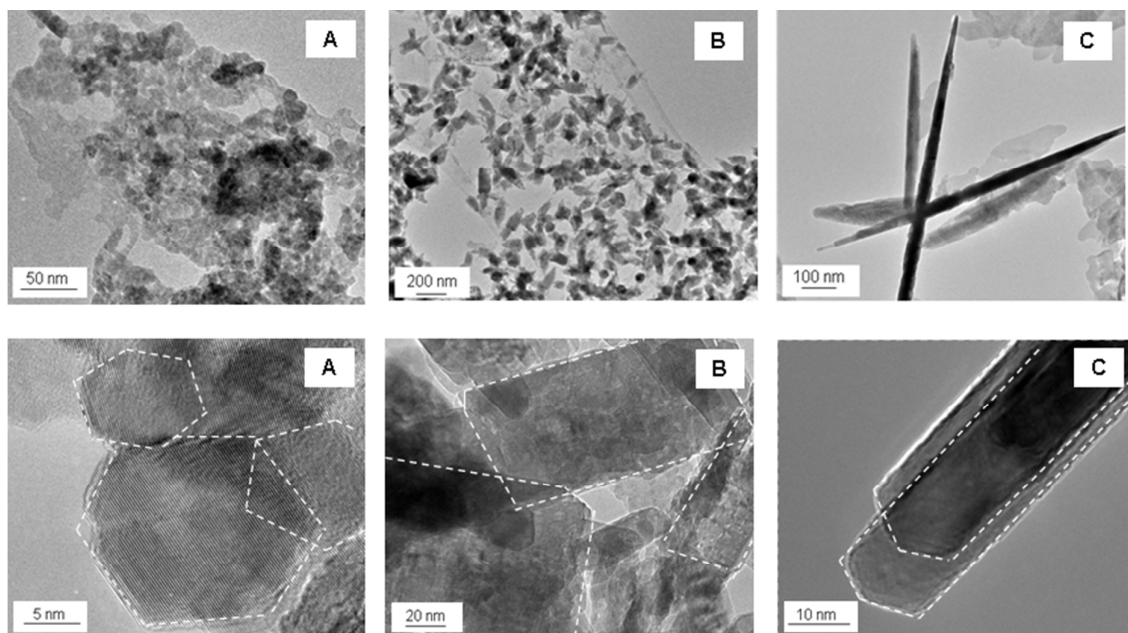


Figure 4.- HR-TEM images and FFT diffraction patterns (from locations marked with a red colour box) corresponding to samples A, B, and C.

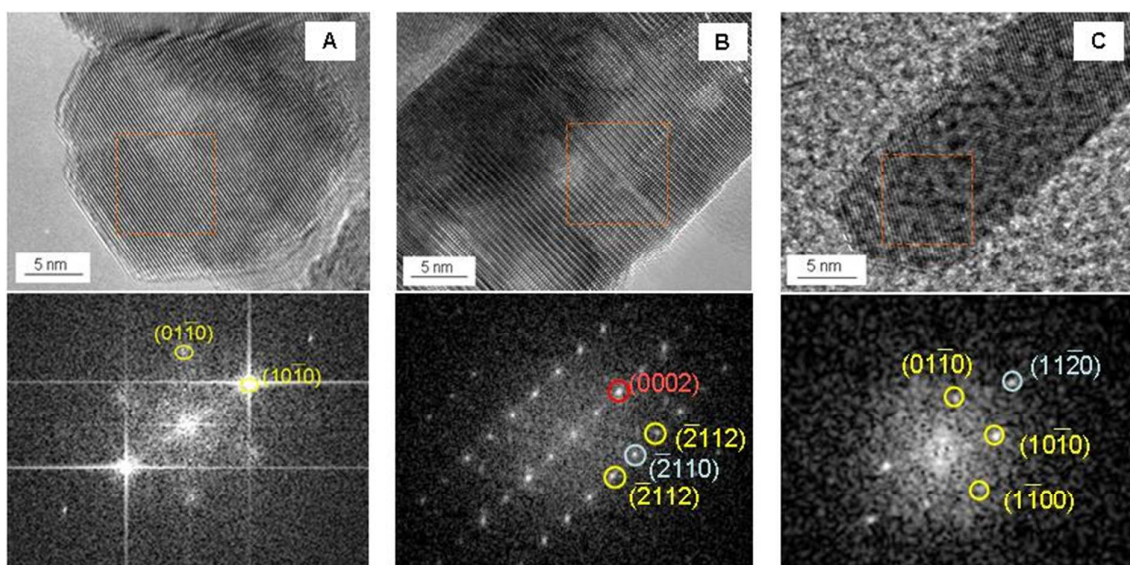


Figure 5.- Density of states of VB and CB of the fully hydrated nonpolar ($10\bar{1}0$) and ($11\bar{2}0$) facets (green and blue), and of the polar (0001) and ($000\bar{1}$) planes (violet and red).

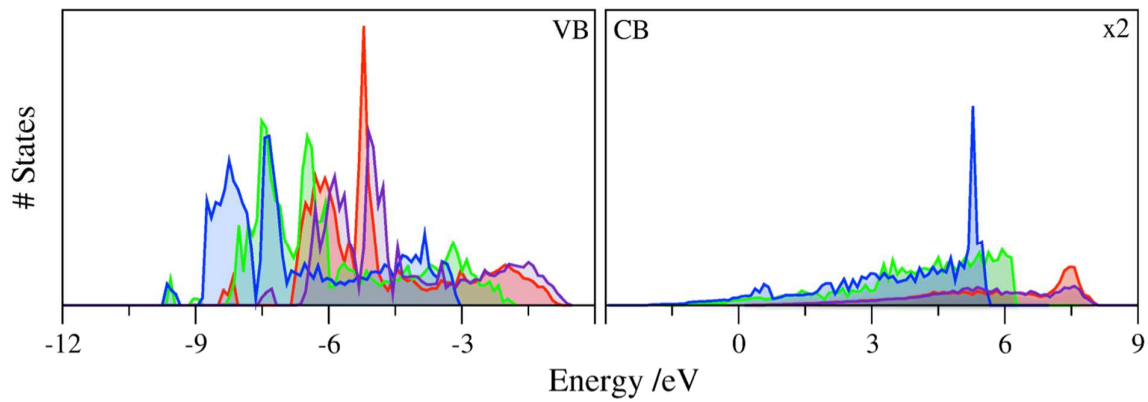


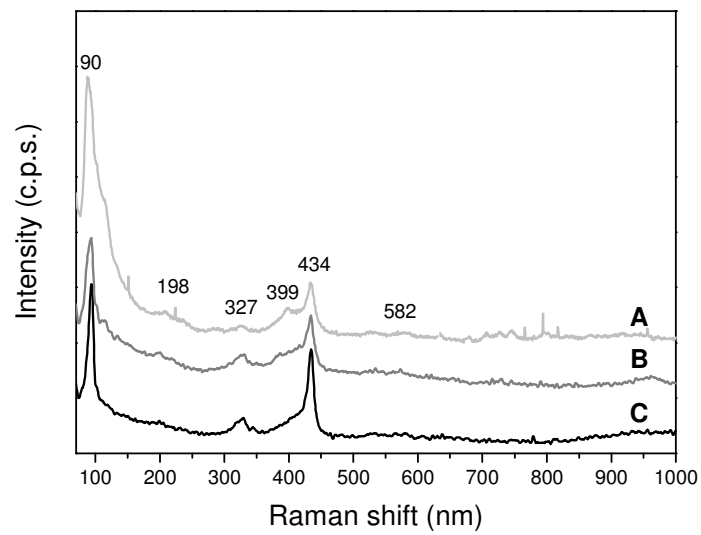
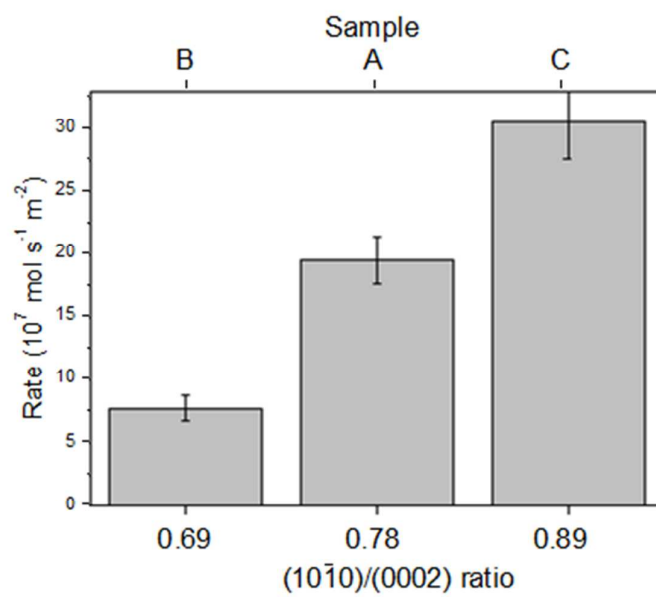
Figure 6.- Raman spectra for samples **A**, **B**, and **C**

Figure 7.- Normalized (per surface area) isopropanol photooxidation rate for samples **A**, **B**, and **C**.



References

- (1) Mang, A.; Reimann, K.; Rübenacke, S.; *Solid State Commun.* **1995**, 94, 251-254.
- (2) Reynolds, D. C.; Look, D. C.; Jogai, B.; Litton, C. W.; Cantwell, G.; Harsch, W. C.; *Phys. Rev. B* **1999**, 60, 2340-2344.
- (3) Djurisic, A. B.; Leung, Y. H.; *Small* **2006**, 2, 944-961.
- (4) Van de Walle, C. G.; Janotti, A.; *Rep. Prog. Phys.* **2009**, 72, 126501.
- (5) Goldberger, J.; Sirbuly, D. J.; Law, M.; Yang, P.; *J. Phys. Chem. B* **2005**, 109, 9-14.
- (6) Kind, H.; Yan, H. Q.; Messer, B.; Law, M.; Yang, P. D.; *Adv. Mater.* **2002**, 14, 158.
- (7) Bagnall, D. M.; Chen, Y. F.; Zhu, Z.; Yao, T.; Koyama, S.; Shen, M. Y.; Goto, T.; *Appl. Phys. Lett.* **1997**, 70, 2230-2232.
- (8) Colvin, V. L.; Schlamp, M. C.; Alivisatos, A. P.; *Nature* **1994**, 370, 354-357.
- (9) Huang, M. H.; Mao, S.; Feick, H.; Yan, H. Q.; Wu, Y. Y.; Kind, H.; Weber, E.; Russo, R.; Yang P. D.; *Science* **2001**, 292, 1897-1899.
- (10) Rout, C. S.; Raju, A. R.; Govindaraj, A.; Rao, C. N. R.; *Solid State Commun.* **2006**, 138, 136-138.
- (11) Göpel, W.; *Prog. Surf. Sci.* **1985**, 20, 9-103.
- (12) Polarz, S.; Roy, A.; Lehmann, M.; Driess, M.; Kruis, F. E.; Hoffmann, A.; Zimmer, P.; *Adv. Func. Mater.* **2007**, 17, 1385-1391.
- (13) Wang, Z. L.; Song, J. H.; *Science* **2006**, 312, 242-246.
- (14) Duran, P.; Capel, F.; Tartaj, J.; Moure, C.; *Adv. Mater.* **2002**, 14, 137-141.
- (15) Gnichwitz, J. F.; Marczak, R.; Werner, F.; Lang, N. N.; Jux, N.; Guldi, D. M.; Peukert, W.; Hirsch, A.; *J. Am. Chem. Soc.* **2010**, 132, 17910-17920.
- (16) Marczak, R.; Werner, F.; Ahmad, R.; Lobaz, V.; Guldi, D. M.; Peukert, W.; *Langmuir* **2011**, 27, 3920-3929.
- (17) O'Regan, B.; Grätzel, M.; *Nature* **1991**, 353, 737-739.
- (18) Wöll, C.; *Prog. Surf. Sci.* **2007**, 82, 55-120.
- (19) Nieuwenhuizen, P. J.; *Appl. Catal. A* **2001**, 207, 55-120.
- (20) Polarz, S.; Strunk, J.; Ischenko, V.; van den Berg, M. W. E.; Hinrichsen, O.; Muhler, M.; Driess, M.; *Angew. Chem. Int. Ed.* **2006**, 45, 2965-2969.
- (21) French, S. A.; Sokol, A. A.; Bromley, S. T.; Catlow, C. R. A.; Rogers, S. C.; King, F.; Sherwood, P.; *Angew. Chem. Int. Ed.* **2001**, 40, 4437-4440.
- (22) Kurtz, M.; Strunk, J.; Hinrichsen, O.; Muhler, M.; Fink, K.; Meyer, B.; Wöll, C.; *Angew. Chem. Int. Ed.* **2005**, 44, 2790-2794.

-
- (23) Meyer, B.; Marx, D.; Dulub, O.; Diebold, U.; Kunat, V.; Langenberg, D.; Wöll, C.; *Angew. Chem. Int. Ed.* **2004**, 43, 6642-6645.
- (24) Rodriguez, J. A.; Maiti, A.; *J. Phys. Chem. B* **2000**, 104, 3630-3638.
- (25) Jirsak, T.; Dvorak, J.; Rodriguez, J. A.; *J. Phys. Chem. B* **1999**, 103, 5550-5559.
- (26) Dvorak, J.; Jirsak, T.; Rodriguez, J. A.; *Surf. Sci.* **2001**, 479, 155-168.
- (27) Hinrichsen, O.; Kochlöfl, K.; Muhler, M.; in *Handbook of Heterogeneous Catalysis* 2nd ed. (Eds: G. Ertl, H. Knözinger, J. Weitkamp) VCH: Weinheim, Germany, **2008**.
- (28) Wang, Y.; Kováčik, R.; Meyer, B.; Kotsis, K.; Stodt, D.; Stämmeler, V.; Qiu, H.; Träger, F.; Langenberg, D.; Muhler, M.; Wöll, C.; *Angew. Chem. Int. Ed.* **2007**, 46, 7315-7318.
- (29) Girol, S.; Strunskus, T.; Muhler, M.; Wöll, C.; *J. Phys. Chem. B* **2004**, 108, 13736-13745.
- (30) Messori, M.; Vaccari, A.; *J. Catal.* **1994**, 150, 177-185.
- (31) Sakthivel, S.; Neppolian, B.; Shankar, M. V.; Arabindoo, B.; Palanichamy, M.; Murugesan, V.; *Sol. Energy Mater. Sol. Cells* **2003**, **77**, 65-82.
- (32) Kulkarni, D.; Wachs, I. E.; *Appl. Catal. A: General* **2002**, 237, 121-137.
- (33) McLaren, A.; Valdes-Solis, T. Li G.; Tsang, S. C.; *J. Am. Chem. Soc.* **2009**, 131, 12540-12541.
- (34) Wagata, H.; Katsumata, K.; Ohashi, N.; Sakai, M.; Nakajima, A.; Fujishima, A.; Okada, K.; Matsushita, N.; *Photochem. Photobiol.* **2011**, 87, 1009-1015.
- (35) Pauporte, T.; Rathousky, J.; *J. Phys. Chem. C* **2007**, 111, 7639-7644.
- (36) Daneshvar, N.; Salari, D.; Khataee, A. R.; *J. Photochem. Photobiol. A: Chem.* **2004**, 162, 317-322.
- (37) Tian, Z. R.; Voigt, J. A.; Liu, J.; McKenzie, B.; McDermott, M. J.; Rodriguez, M. A.; Konishi, H.; Xu, H.; *Nat. Mater.* **2003**, 2, 821-826.
- (38) Kormann, C.; Bahnemann, D. W.; Hoffmann, M. R.; *Environ. Sci. Technol.* **1988**, 22, 798-806.
- (39) Maeda, K.; Domen, K.; *Chem. Mater.* **2010**, 22, 612-623.
- (40) Khodja, A. A.; Sehili, T.; Pilichowski, J. F.; Boule, P.; *J. Photochem. Photobiol. A: Chem.* **2001**, 141, 231-239.
- (41) Xu, L.; Hu, Y. L.; Pelligra, C.; Chen, C. H.; Jin, L.; Huang, H.; Sithambaram, S.; Aindow, M.; Joesten, R.; Suib, S. L.; *Chem. Mater.* **2009**, 21, 2875-2885.
- (42) Kislov, N.; Lahiri, J.; Verma, H.; Goswami, D. Y.; Stefanakos, E.; Batzill, M.; *Langmuir* **2009**, 25, 3310-3315.

-
- (43) Li, G. R.; Hu, T.; Pan, G. L.; Yan, T. Y.; Gao, X. P.; Zhu H., Y.; *J. Phys. Chem. C* **2008**, 112, 11859-11864.
- (44) Vayssieres, L.; *Adv. Mater.* **2003**, 15, 464-466.
- (45) Lizandara-Pueyo, C.; Siroky, S.; Wagner, M. R.; Hoffmann, A.; Reparaz, J. S.; Lehmann, M.; Polarz, S.; *Adv. Func. Mater.* **2011**, 21, 295-304.
- (46) Wang, Z. L.; *ACS Nano* **2008**, 2, 1987-1992.
- (47) Lizandara-Pueyo, C.; Morant-Minana, M. C.; Wessig, M.; Krumm, M.; Mecking, S.; Polarz S.; *RSC Adv.* **2012**, 2, 5298-5306.
- (48) Yang, J.; Wang, J.; Li, X.; Lang, J.; Liu, F.; Yang, L.; Zhai, H.; Gao, M.; Zhao, X.; *J. Alloys Compd.* **2012**, 528, 28-33.
- (49) Polarz, S.; Roy, A.; Merz, M.; Halm S.; Schröder D.; Schneider L.; Bacher, G.; Kruis, F. E.; Driess, M.; *Small* **2005**, 5, 540-552.
- (50) Lauritsen, J. V.; Porsgaard, S.; Rasmussen, M. K.; Jensen, M. C. R.; Bechstein, R.; Meinander, K.; Clausen, B. S.; Helveg, S.; Wahl, R.; Kresse, G.; Besenbacher, F.; *ACS Nano* **2011**, 5, 5987-5994.
- (51) Valtiner, M.; Todorova, M.; Grundmeier, G.; Neugebauer, J.; *Phys. Rev. Lett.* **2009**, 103, 065502.
- (52) Colón, G.; Sampedro, P.; Fernández-García, M.; Chen, H.; Hanson, J. C.; Rodriguez, J. A.; *Langmuir* **2008**, 24, 11111-11118.
- (53) Richard, C.; Bosquet, F.; Pilichowski, J.-F.; *J. Photochem. Photobiol. A: Chem.* **1997**, 108, 45-49.
- (54) Richard, C.; Boule, P.; *Sol. Energy Mater. Sol. Cells* **1995**, 38, 431-440.
- (55) Xu, F.; Zhang, P.; Navrotsky, A.; Yuan, Z. Y.; Ren, T. Z.; Halasa, M.; Su B. L.; *Chem. Mater.* **2007**, 19, 5680-5686.
- (56) Le Bail, A.; Duroy, H.; Fourquet, J. L.; *Mater. Res. Bull.* **1988**, 23, 447-452.
- (57) Goniakowski, J.; Finocchi F.; Noguera C.; *Rep. Prog. Phys.* **2008**, 71, 016501.
- (58) Noguera, C.; *J. Phys.: Condens. Matter* **2000**, 12, R367.
- (59) Kresse, G.; Dulub, O.; Diebold, U.; *Phys. Rev. B* **2003**, 68, 245409.
- (60) Dulub, O.; Diebold, U.; Kresse, G.; *Phys. Rev. Lett.* **2003**, 90, 016102.
- (61) Stämmler, V.; Fink, K.; Meyer, B.; Marx, D.; Kunat, M.; Burghaus, U.; Gil-Girol, S.; Wöll, C.; *Phys. Rev. Lett.* **2003**, 90, 106102.
- (62) Kunat, M.; Gil-Girol, S.; Burghaus, U.; Wöll, C.; *J. Phys. Chem. B* **2003**, 107, 14350-14356.

-
- (63) Becker, T.; Hövel, S.; Kunat, M.; Boas, C.; Burghaus, U.; Wöll, C.; *Surf. Sci.* **2001**, 486, 502-506.
- (64) Viñes, F.; Iglesias-Juez, A.; Illas, F.; Fernández-García, M. *J. Phys. Chem. C* **2014**, 118, 1492.
- (65) Kresse, G.; Dulub, O.; Diebold, U.; *Phys. Rev. B* **2003**, 68, 245409.
- (66) Meyer, B.; Marx, D.; *Phys. Rev. B* **2003**, 67, 035403.
- (67) Wander, A.; Schedin, F.; Steadman, P.; Norris, A.; McGrath, R.; Turner, T. S.; Thornton, G.; Harrison, N. M.; *Phys. Rev. Lett.* **2001**, 86, 3811-3814.
- (68) Wander, A.; Harrison, N. M.; *Surf. Sci.* **2000**, 457, L342-L346.
- (69) Moreira, N. H.; Dolgonos, G.; Aradi, B.; da Rosa, A. L.; Frauenheim, T.; *J. Chem. Theo. Comput.* **2009**, 5, 605-614.
- (70) Li, H.; Schirra, L. K.; Shim, J.; Cheun, H.; Kippelen, B.; Monti, O. L. A.; Bredas, J.-L.; *Chem. Mater.* **2012**, 24, 3044-3055.
- (71) Nénon, S.; Méreau, R.; Salman, S.; Castet, F.; Regemorter, T. V.; Clima, S.; Beljonne, D.; Cornil, J.; *J. Phys. Chem. Lett.* **2012**, 3, 58-63.
- (72) Cooke, D. J.; Marmier, A.; Parker, S. C.; *J. Phys. Chem. B* **2006**, 110, 7985-7991.
- (73) Labat, F.; Ciofini, I.; Adamo, C.; *J. Chem. Phys.* **2009**, 131, 044708.
- (74) Meyer, B.; Rabaa, H.; Marx, D.; *Phys. Chem. Chem. Phys.* **2006**, 8, 1513-1520.
- (75) Wander, A.; Harrison, N. M.; *J. Chem. Phys.* **2001**, 115, 2312-2316.
- (76) Meyer, B.; Marx, D.; Dulub, O.; Diebold, U.; Kunat, M.; Langenberg, D.; Wöll, C. *Angew. Chem. Int. Ed.* **2004**, 43, 6642.
- (77) Dulub, O.; Meyer, B.; Diebold, U. *Phys. Rev. Lett.* **2005**, 95, 136101.
- (78) Kresse, G.; Furthmüller, J.; *Phys. Rev. B* **1996**, 54, 11169-11186.
- (79) Blöchl, P. E.; *Phys. Rev. B* **1994**, 50, 17953-17979.
- (80) Perdew, J. P.; Burke, K.; Ernzerhof, M.; *Phys. Rev. Lett.* **1996**, 77, 3865-3868.
- (81) Alkauskas, A.; Pasquarello, A.; *Phys. Rev. B* **2011**, 84, 125206.
- (82) Moreira, N. H.; Dogonos, G.; Aradi, B.; da Rosa A. L.; Frauenheim, T. *J. Chem. Theo. Comput.* 2009, 5, 605.
- (83) Becke, A. D. *J. Chem. Phys.* 1993, 98, 5648.
- (84) Patterson, C. H. *Phys. Rev. B* 2006, 74, 144432.
- (85) Demiroglu, I.; Tosoni, S.; Illas, F.; Bromley, S. T. *Nanoscale* **2014**, 6, 1181.
- (86) Viñes, F.; Sousa, C.; Liu, P.; Rodriguez, J. A.; Illas, F.; *J. Chem. Phys.* **2005**, 122, 174709.

-
- (87) Marana, N. L.; Longo, V. M.; Longo, E.; Martins, J. B. L.; Sambrano, J. R.; *J. Phys. Chem. A* **2008**, 112, 8958-8963.
- (88) Karazhanov, S. Z.; Ravindran, P. R.; Kjekshus, A.; Fjellvag, H.; Grossner, U.; Svensson, B. G.; *J. Appl. Phys.* **2006**, 100, 043709.
- (89) Decremps, F.; Datchi, F.; Saitta, A. M.; Polian, A.; Pascarelli, S.; Di Cicco, A.; Itié, J. P.; Baudelet, F.; *Phys. Rev. B* **2003**, 68, 104101.
- (90) Feng, X.; Feng, L.; Jin, M.; Zhai, J.; Jiang, L.; Zhu, D.; *J. Am. Chem. Soc.* **2004**, 126, 62-63.
- (91) Uskokovic, V.; Drofenik, M.; *Surf. Rev. Lett.* **2005**, 12, 239-277.
- (92) Henderson, M. A.; *Surf. Sci. Rep.* **2011**, 66, 185-297.
- (93) Zhang, L.; Ying, L.; Wang, C.; Lun, N.; Qui, Y.; Xing, D.; *J. Phys. Chem. C* **2010**, 114, 9561-9568.
- (94) Kubacka, A.; Fernández-García, M.; Colón, G.; *Chem. Rev.* **2012**, 112, 1555-1614.
- (95) Iglesias-Juez, A.; Kubacka, A.; Colón, G.; Fernández-García, M.; "Photocatalytic Nanooxides: the case of TiO₂ and ZnO" in *Catalysis by Nanoparticles (New and of the Future Developments in Catalysis Series)*. Editor S. Suib. Elsevier, Amsterdam (**2013**), ISBN: 978-0-44-453874-1).
- (96) Schlesinger R.; Xu, Y.; Hofmann, O.T.; Winkler, S.; Frisch, J.; Niederhausen, J.; Vollmer, A.; Blumstengel, S.; Henneberger, F.; Rinke, P.; Scheffler, M.; Koch, N.; *Phys. Rev. B* **2013**, 87, 155311.
- (97) Gutmann, S.; Conrad, M.; Wolak, M. A.; Beerbom, M. M.; Schlaf, R.; *J. Appl. Phys.* **2012**, 111, 123710.
- (98) Hofmann, O. T.; Deinert, J.-C.; Xu, Y.; Rinke, P.; Stähler, J.; Wolf, M.; Scheffler, M.; *J. Chem. Phys.* **2013**, 139, 174701.
- (99) Tisdale, W. A.; Muntwiler, M.; Norris, D. J.; Aydil, E. S.; Zhu, X.-Y.; *J. Phys. Chem. C* **2008**, 112, 14682-14692.
- (100) Lange, I.; Reiter, S.; Pätzelt, M.; Zykov, A.; Nefedov, A.; Hildebrandt, J.; Hecht, S.; Kowarik, S.; Wöll, C.; Heimel, G.; Neher, D.; *Adv. Func. Mater.* **2014**, 24, 7014-7024.